Nature Communications

https://doi.org/10.1038/s41467-026-70662-2

Article in Press

Asymmetric global urban cooling potential demands accelerated and context-specific actions

Received: 19 September 2025

Accepted: 25 February 2026

Cite this article as: Ding, X., Fan, Y., Zhao, Y. *et al.* Asymmetric global urban cooling potential demands accelerated and context-specific actions. *Nat Commun* (2026). https://doi.org/10.1038/s41467-026-70662-2

Xiaotian Ding, Yifan Fan, Yongling Zhao, Diana Ürge-Vorsatz, Jian Ge & Jan Carmeliet

Asymmetric global urban cooling potential demands accelerated and context-specific actions

Xiaotian Ding[1,2,3,4], Yifan Fan[1,4,5*], Yongling Zhao[3*], Diana Ürge-Vorsatz[6], Jian Ge[1,4,5], Jan Carmeliet[3]

[1]Department of Architecture, College of Civil Engineering and Architecture, Zhejiang University, Hangzhou, 310058, China
[2]Center for Balance Architecture, Zhejiang University, Hangzhou, 310028, China
[3]Department of Mechanical and Process Engineering, ETH Zurich, Zurich, Switzerland
[4]International Research Center for Green Building and Low-Carbon City, International Campus, Zhejiang University, Haining, China
[5]The Architectural Design & Research Institute of Zhejiang University Co., Ltd., Hangzhou, 310028, China
[6]Central European University, Vienna, Austria

*Correspondence to: Yifan Fan, email: yifanfan@zju.edu.cn; Yongling Zhao, email: yozhao@ethz.ch

Abstract

Rising urban temperatures and heat extremes pose an urgent global challenge, yet the potential for mitigating excessive urban heat–particularly at the global scale–remains unclear. Here, we quantify the cooling potential across 2,265 cities worldwide by the 2050s using validated urban climate simulations. Cooling effects are quantified as the reduction in the summer average wet-bulb globe temperature (WBGT) and heat danger hours (HDH; WBGT > 31.4 °C) under the combined implementation of reflective surfaces, green transformation, and anthropogenic heat reduction. We show a distinct spatial asymmetry: while the cooling potential increases with latitude, primarily due to greater cooling from reflective surfaces, the highest heat risk is concentrated in low- to mid-latitude regions (10°N-40°N). In these high-risk regions, combined mitigation is more effective at night, reducing HDH by an average of 37%, whereas daytime heat

is mitigated to a lesser extent (11%). These asymmetries underscore the need for context-specific strategies—particularly accelerated action and localized innovation for low-latitude humid regions—as well as the integration of city-scale planning with targeted daytime heat risk interventions.

Introduction

Urban temperatures are generally higher than those in surrounding rural areas due to the changes in surface energy balance caused by urban development, a phenomenon known as the urban heat island (UHI) effect[1]. Moreover, increasingly frequent extreme heat events are expected to exacerbate heat risk[2,3]. By the 2050s, the frequency of urban heat extremes is projected to be 2.5 times greater than that in 2023 (**Supplementary Fig. 1**), based on climate projections from the coupled model intercomparison project phase 6 (CMIP) under a high-emission scenario (SSP 5-8.5), which represents the most aggressive pathway combining Representative Concentration Pathways (RCPs) and Shared Socioeconomic Pathways (SSPs). As the urban population continues to grow and cities expand[4], these cascading effects pose heat-related health risks[5–8] and socioeconomic burdens[9–12] of varying severity for cities worldwide.

Urban heat arises from a complex interplay between background climate conditions and city-specific urban characteristics[13,14], which have been studied at both regional[15,16] and global scales[16–18]. While these studies have primarily offered insights into the causes of urban heat, understanding the effectiveness and underlying mechanisms of urban heat mitigation strategies across different climates remains incomplete, as much of the literature has focused on localized case studies[19,20]. This suggests a pressing need to broaden the scope of research to the global scale, with the goal of building a more comprehensive body of knowledge that can be generalized across diverse climates and urban forms—ultimately supporting the transformation of cities towards greater resilience[19,21,22].

Specifically, the root cause of the urban heat island effect lies in changes in the surface energy balance within cities [1]. Typical heat mitigation strategies—such as the deployment of reflective materials and the implementation of nature-based solutions to conserve and restore natural ecosystems—aim to reduce urban heat by modifying the surface energy balance. These interventions operate through increased reflection of incoming solar radiation[23,24], enhanced evapotranspiration[25], additional shading effects[20], and reduced anthropogenic heat emissions[26,27]. While existing studies have evaluated their effectiveness in cooling ambient temperature[19,28], a systematic understanding of their specific impacts on individual components of the surface energy balance—and how these impacts, along with the efficiency of translating energy modifications into actual cooling[29,30], vary across different climatic contexts—remains limited.

Here, we assess the potential for mitigating future urban heat by the 2050s across 2,265 global cities using a mesoscale numerical weather prediction model. Specifically, we employ the Weather Research and Forecasting (WRF) model coupled with urban canopy parameterizations to simulate the cooling potential from heat mitigation measures. The model is first validated against weather station observations and then driven by future climate and urban expansion projections under a high-emission pathway (CMIP6 SSP 5-85). The cooling potential is quantified as the reduction in the five-summer average wet-bulb globe temperature ($WBGT$)[18,31]—a metric that captures the

combined effects of air temperature and humidity on human thermal stress—by comparing the baseline case (without mitigation) with the mitigation cases (with mitigation). For each city, we evaluate the integrated effects of three physics-representative mitigation strategies: deployment of reflective roofs/pavements, green transformation (preserving and restoring green areas), and anthropogenic heat reduction by optimizing air conditioning (AC) systems (increasing both the efficiency and the setpoint temperature). To further elucidate the underlying mechanisms driving variations in urban heat mitigation effectiveness, model outputs are analyzed to quantify the efficacy of these mitigation measures in modifying surface heat fluxes, as well as the contributions of these changes to the resulting cooling effect across regions and climates. A detailed description of the model, used datasets, and analytical procedures is provided in the Methods section.

Results

Asymmetric cooling potential in future heat extremes

The results reveal a pronounced spatial asymmetry in the reduction of exposure to heat extremes, quantified by reduced summer heat danger hours when the $WBGT$ exceeds the "danger" threshold[32] of 31.4 °C ($\Delta HDH_{31.4}$, see Methods). The spatial distribution of the baseline $HDH_{31.4}$ (i.e., without heat mitigation) shows that cities between 10° N and 40° N generally experience substantial heat risks (**Fig. 1a, b**), with average $HDH_{31.4}$ values of 515 and 702 for dry and wet climate cities, respectively. In contrast, the cities north of 40° N and south of 10° N experience significantly lower $HDH_{31,4}$ values, averaging only 69. When the "severe warning" threshold (29 °C)[32] is used, this high-risk zone expands to 10° S–40° N, with average $HDH_{31.4}$ values of 808 and 1200 for dry and wet climate cities, respectively, whereas only 167 HDH_{29} are observed in the remaining lower-risk latitudinal bands (**Supplementary Fig. 5a, b**).

This non-equatorially symmetric distribution likely reflects the differences in background climate and the amplified warming from the uneven land–ocean distribution between the Northern and Southern Hemispheres[33]. Cities located between 20° and 40° absolute latitude experience more intense and prolonged summer solar irradiance than equatorial cities, exacerbating urban overheating. Climate wetness also plays a key role: within the same latitudinal band, cities in wet climates consistently present higher $HDH_{31.4}$ ($p<0.01$) and HDH_{29} ($p<0.01$) values than their dry-climate counterparts[18].

In contrast, the effectiveness of combined mitigation measures in addressing heat extremes exhibits an opposing variation across latitudes (**Fig. 1a-d**). In the high-risk zone (10° N–40° N), $HDH_{31.4}$ can be mitigated by an average of 97 hours in dry climates and 124 hours in wet climates, corresponding to approximately 22% and 20%, respectively, of the respective baseline values (considering only cities in which the baseline $HDH_{31.4}$ exceeds zero.). Moreover, outside this region, the reduction averages 22 hours, accounting for 45% of the baseline. For HDH_{29}, the reduction reaches 101 (14%) and 138 (18%) in dry-climate and wet-climate cities, respectively, within the high-risk zone (10° S–40° N; **Supplementary Fig. 5c, d**). In the low-risk region, the

reduction is smaller in absolute terms—43 hours on average—but represents a relatively larger share of the baseline (37%).

In addition, a distinct diurnal asymmetric pattern is observed between the occurrence of heat extremes and the cooling effectiveness. The number of heat danger hours tends to increase after sunrise, peaking between 15:00 and 16:00 local time before declining into the evening (**Fig. 1e**). Mitigation efforts offer limited relief during peak daytime hours, achieving an average reduction of 11% (21 hours) in $HDH_{31.4}$ (6% in HDH_{29}) relative to baseline conditions in high-risk zones (**Fig. 1f and Supplementary Fig. 5e, f**). In contrast, substantially greater reductions are observed during the evening (after 19:00) and early morning (before 8:00) (**Fig. 1f**), reflecting strong mitigation impacts during the nighttime (20:00–04:00) and transitional periods (16:00–20:00 and 04:00–08:00). At night, the combined strategies reduce $HDH_{31.4}$ by 37% (55 hours) and HDH_{29} by 21% (56 hours), demonstrating their high effectiveness in alleviating nighttime heat stress in urban populations during physiologically vulnerable hours[34].

Asymmetric cooling potential in future urban heat stress

Consistent with the spatial pattern of reduced heat extremes, the cooling potential—represented by the mean $\Delta WBGT$ for the 2050s—also exhibits a pronounced latitudinal dependence that contrasts with the pattern observed under baseline climate conditions (i.e., without heat mitigation). The cooling potential increases with latitude and is generally stronger at night than during the day (**Fig. 2a, c**). In contrast, cities near the tropics (absolute latitude, $|lat| \approx 23.5°$) generally experience higher levels of heat stress than those at higher latitudes, particularly in regions with wetter climates (i.e., summer precipitation $P_s \geq 570$ mm), as shown in **Fig. 2b, d**.

The cooling effect peaks at 0.65 ± 0.40 °C (mean ± SD) between 40°–60° absolute latitude during the day (**Fig. 2a**) and 0.91± 0.57 °C between 30°–50° at night (**Fig. 2c**). In comparison, cities located in lower latitude regions ($|lat| \leq 20°$) tend to exhibit limited cooling potential, with $\Delta WBGT$ values of 0.17 ± 0.10 °C during the day and 0.45 ± 0.29 °C at night. This latitudinal and diurnal pattern is primarily substantiated by simulations using an alternative driving climate (see Methods), in which the maximum daytime $\Delta WBGT$ (0.58 ± 0.33 °C) occurs between 50° and 60° absolute latitude, and the maximum nighttime reduction (0.94 ± 0.53 °C) is between 30° and 40° (**Supplementary Fig. 2a, c**).

This enhanced nighttime cooling effect results in an average $\Delta WBGT$ of 0.37 °C greater than that during the day. This likely reflects the substantial mitigation of the nighttime urban heat island effect achieved through the green transformation strategy (incorporating sustainable planning to guide urban development towards preserving and restoring vegetated areas[35,36]). Compared with rapid, unconstrained urban expansion pathways, this intervention increases vegetation cover and reduces the extent of urban surfaces to restore key ecosystem functions. In addition to enhancing evapotranspiration, it naturally decreases urban heat storage capacity and anthropogenic heat emissions—both of which are primary drivers of the UHI effect. As a result, the UHI effect is

mitigated, particularly during nighttime hours when its intensity is typically at its peak[37,38].

This latitudinal dependence is also evident in surface temperature reduction (ΔT_s), which has a strong correlation with incoming solar exposure—both in terms of intensity and duration (**Supplementary Fig. 3**). Moreover, these reductions are typically suppressed in wetter regions, where precipitation and cloud cover are more frequent[39]. These estimated patterns of ΔT_s are consistent with prior findings indicating that latitudinal variability in the response of the local thermal environment to land cover changes—such as urbanization[40] and deforestation[41,42]—is correlated primarily with variations in the surface radiation budget and precipitation patterns[42,43]. However, the influence of climate wetness on $WBGT$ reduction is relatively moderate (**Fig. 2a, c**), indicating a more direct influence of climate wetness on surface temperature change than on the actual reduction in heat stress, as measured by $\Delta WBGT$.

Cooling patterns explained by surface energy flux changes

To elucidate the underlying influence mechanisms in the observed global patterns of urban heat mitigation potential, we apply a multiple linear regression approach to quantify how changes in surface energy balance components are related to the overall cooling effect in summer (see Methods).

During the daytime, the cooling effect is driven primarily by reductions in surface net radiation (ΔR_n), lowering $WBGT$ by 0.44 ± 0.30 °C (**Fig. 3a**). Meanwhile, the heat conducted into urban ground and building surfaces (ΔQ_G) is reduced, which is likely attributed to reduced heat storage and increased reflectance. This change may indicate that more available energy is being converted to heat up the near-surface atmosphere through turbulent heat fluxes rather than being stored in urban surfaces, a mechanism also observed in previous studies[44,45]. Moreover, the reduced anthropogenic heat (ΔQ_F) and the enhanced transpiration effect—represented by an increased fraction of latent heat $\Delta\beta = \Delta(Q_E/A^*)$, where A^* denotes the surface available energy ($A^* = R_n + Q_G + Q_F$)—both partially contribute to the overall cooling effect.

At night, the dominant drivers shift, with the cooling effect driven primarily and jointly by reductions in both anthropogenic heat (ΔQ_F) and net radiation (ΔR_n), each contributing to $\Delta WBGT$ values of 0.55 ± 0.41 °C and 0.31 ± 0.21 °C, respectively (**Fig. 3b**). Compared with that during the day, the sensitivity of $\Delta WBGT$ to ΔQ_F and ΔQ_G increases more than sixfold, from approximately 0.010 to 0.065 $K \cdot W^{-1} \cdot m^2$ (**Supplementary Table 4**), highlighting that reducing anthropogenic heat and heat storage is substantially more effective for mitigating nighttime heat than daytime cooling. This elevated nighttime sensitivity likely results from the amplified thermal response within the shallow nocturnal boundary layer[46,47]. Moreover, the sensitivity of $\Delta WBGT$ to ΔR_n decreases by approximately 30% to 0.031 $K \cdot W^{-1} \cdot m^2$ (**Supplementary Table 4**), indicating a lasting cooling effect from reduced daytime radiative heat gain.

On the basis of this diagnostic framework, we further evaluate the efficacy of individual mitigation measures in altering surface energy fluxes and their associated cooling impacts across latitude regions and climates. The results indicate that reflective cooling functions mainly through reducing the net radiation (ΔR_n) at urban surfaces, which has a clear latitudinal dependence (**Fig. 4a, e**), likely due to the differences in the availability of direct solar radiation across latitudes. Moreover, this mechanism tends to be more effective in dry climates, where clearer skies allow greater modulation of net radiation than in wetter and cloudier regions—a pattern similar to the response observed in surface temperature (**Supplementary Fig. 3**). Among these energy components, ΔR_n contributes the most to the daytime temperature and accounts for a major part of the nighttime temperature reduction, thereby playing a key role in shaping the latitudinal pattern observed in $\Delta WBGT$ (**Fig. 2b, d**).

Our green transformation strategy enhances urban cooling through both increased vegetated cover—promoting shading and evapotranspiration—and a reduced urban fraction that decreases heat storage and anthropogenic heat emissions. However, owing to the tiling approach implemented in the WRF land surface model[48], tree shading is represented only in rural areas and is not explicitly accounted for within urban canyons. The modeled green transformation more closely resembles the addition of large urban parks rather than street trees, which differs from microclimate modeling approaches that capture the shading effects of street trees on urban surfaces[49] (**Fig. 4a**). The transpiration effect from additional vegetation is most pronounced during the day when stimulated by solar radiation, lowering ambient temperatures but simultaneously increasing atmospheric moisture[20]. Influenced by these competing effects, the contribution to $WBGT$ reduction is relatively modest during the day, as indicated by the influence of $\Delta\beta$ (**Fig. 4d**). In contrast, a reduction in Q_F has a greater cooling effect than other processes (**Fig. 4b, f**), especially at night, when $\Delta WBGT$ is more sensitive to ΔQ_F. The lowered urban heat storage capacity leads to less heat accumulation and subsequent nighttime release, thereby resulting in contrasting contributions to cooling effects between daytime and nighttime (**Fig. 4c, g**). As a result, this strategy is particularly effective at reducing nighttime heat across the entire urban domain (**Supplementary Fig. 6**). This highlights the value of large-scale restoration of natural areas in mitigating nighttime urban heat and underscores the need for spatially optimized implementation of nature-based solutions (e.g., street trees) within urban areas to maximize localized shading effects and enhance daytime cooling at finer spatial scales[20,50].

Meanwhile, increasing the efficiency of AC systems and raising setpoint temperatures have also been found to reduce anthropogenic heat emissions[51,52], as shown in **Supplementary Fig. 7**. Owing to the greater sensitivity of nighttime $\Delta WBGT$ to ΔQ_F, the reduction in anthropogenic heat flux contributes more substantially to nighttime cooling (**Fig. 4b, f**), even though ΔQ_F is slightly greater during the daytime (**Supplementary Fig. 7d**). However, this strategy induces an unexpected compensatory effect, leading to a moderate increase in nighttime ground heat flux (ΔQ_G) (**Fig. 4g**). This response can be attributed to elevated indoor air temperatures due to higher

AC setpoints, which facilitate heat storage within buildings and increase exterior surface temperatures (**Supplementary Fig. 9**). Consequently, this promotes enhanced nocturnal heat release to the ambient environment, partially offsetting the cooling benefits. This trade-off results in the lowest net cooling effect among the evaluated individual strategies (**Supplementary Fig. 6**). Nonetheless, these findings underscore the cooling potential of reducing anthropogenic heat and the importance of technically selective approaches—such as promoting electric vehicles[27,53] that avoid such side effects—as critical pathways for mitigating nighttime heat.

Discussion

The reductions in surface available energy (R_n, Q_F, and Q_G) alter the heat and moisture exchange between urban surfaces and the atmosphere, resulting in changes in surface temperature (ΔT_s), near-surface air temperature (ΔT_a) and humidity (expressed as changes in vapour pressure, Δe_a). A similar latitudinal dependence can be observed for ΔT_s and ΔT_a (**Supplementary Fig. 3 and 10a, b**), consistent with previous observational studies reporting comparable spatial patterns in surface[41,54] and near-surface air temperature[42,43] variations induced by albedo changes following deforestation. These similar latitudinal patterns reflect the close coupling between surface and air temperatures through sensible heat transfer—particularly in drier regions where evapotranspiration is limited[55].

In contrast, the humidity-related component of heat stress (expressed as e_a/γ, where γ is the psychrometric constant[18]) exhibits a slightly different latitudinal distribution pattern, with the maximum reduction shifting towards mid-latitudes ($|lat|$ between 20° and 40°; **Supplementary Fig. 10c, d**). This pattern partly reflects shifts in surface–atmosphere moisture exchange, as evidenced by the moderate equatorward increase in latent heat flux (ΔQ_E; **Supplementary Fig. 8h, j**). Such behavior agrees well with previous findings that the control of surface available energy on evapotranspiration becomes increasingly dominant toward low-latitude tropical and subtropical regions where soil moisture is generally sufficient[56,57]; thus, reductions in available energy lead to greater declines in latent heat flux in these areas[58]. As a result, this difference in the variation in ΔT_a and Δe_a suggests that, compared with $WBGT$, using alternative heat stress metrics that place greater (e.g., wet-bulb temperature[45]) or lesser (e.g., Heat Index[18]) weight on humidity could lead to marginally higher or lower estimates of cooling effectiveness in mid-latitude cities.

Owing to the latitudinal and climate dependence of the cooling effect, spatial asymmetry emerges in terms of exposure to heat extremes and cooling potential: cities experiencing greater heat risk are located primarily in low-to-mid latitude regions between 10° N and 40° N, which exhibit an average potential reduction of ~21% in heat extremes, whereas the greatest mitigation potential (~45%) is projected for cities at higher latitudes. This spatial distribution of projected heat risk is consistent with previous studies[3,59], and the asymmetry may be further amplified by the relatively lower adaptive capacity—(society's ability and willingness to implement mitigation measures) in low-latitude regions, particularly in Africa and Southeast Asia[60]. Consequently, this asymmetry

highlights the urgent need for accelerated action and innovation for cities located in high-risk regions, where conventional strategies may be less effective[61]. Based on our results (**Fig. 4**), in regions facing high heat risk but limited mitigation potential, reflective materials remain the most effective among the three mitigation categories, exerting the largest influence on the surface energy balance and yielding the strongest cooling effect. Therefore, to narrow the spatial asymmetry in cooling potential, enhancing the performance of reflective cooling should be prioritized, for example through the deployment of advanced cool materials that are both highly reflective and emissive[62]. Meanwhile, measures that reduce anthropogenic heat emissions exhibit relatively weak latitude dependence and provide pronounced cooling benefits at night[46], suggesting that their implementation should also be encouraged in these regions.

Furthermore, combined city-scale mitigation is more effective at alleviating nighttime heat stress, reflecting the greater sensitivity of $\Delta WBGT$ to nighttime energy flux changes likely driven by the shallower and more stable nocturnal boundary layer, a mechanism also highlighted in previous studies[46,47,63]. This enhanced nighttime cooling effect—reducing nighttime heat extremes by an average of 37% in high-risk regions—is particularly beneficial for reducing health risks associated with prolonged heat exposure in urban populations by improving sleep quality and supporting recovery from daytime exposure[34]. While mitigating nighttime heat is important for public health, daytime heat poses more immediate risks, especially for vulnerable groups such as outdoor workers[3]. Our results indicate that without accounting for localized cooling effects, such as the shading effect provided by street trees and enhanced ventilation achieved through morphological optimization, the proposed green transformation alone remains insufficient to achieve substantial daytime cooling at city scale. It highlights the importance of advancing multi-scale simulation frameworks to better represent and quantify these cooling benefits across temporal and spatial scales. Moreover, this underscores the need—particularly in areas experiencing pronounced daytime heat exposure—to implement a comprehensive system of city-scale strategies that can deliver lasting cooling across the entire urban area, while localized interventions such as street trees, shading structures and permeable pavements are essential for addressing daytime heat exposure by providing shading effects and evapotranspiration cooling at the microscale[64].

This study provides an assessment of the global potential for future urban heat mitigation using a physics-based modeling framework and highlights the asymmetry in global cooling potential, which calls for context-specific and cross-scale actions that account for regional climatic and geographic differences as well as diurnal variation. Previous regional- or local-scale studies[65–68] that implemented two or more mitigation strategies generally reported overall air temperature reductions of approximately 0.2–2 °C on average throughout the diurnal cycle. It should be acknowledged, however, that ensuring comparability across cities in our assessment required certain assumptions, which might not comprehensively capture the diversity of socioeconomic contexts or the varying degrees of technological and policy readiness that affect practical implementation. These dimensions should be carefully considered when formulating the most

practical and effective heat mitigation strategies for different urban settings. Potential trade-offs of mitigation measures at localized areas—such as excessive reflection associated with reflective materials[69,70], as well as reduced ventilation and greater nighttime heat retention caused by dense tree canopies[71,72]—should be carefully evaluated and minimized through innovative materials and design strategies to ensure that cooling strategies deliver overall net benefits across seasons and throughout diurnal cycles. Building on the established understanding of global urban heat mitigation potential, city-specific investigations that integrate detailed climatic and socioeconomic factors—such as demographics, health vulnerability, and economic capacity across scales[73], which jointly shape exposure [74] and adaptive capacity[75]—provide a concrete pathway for translating this knowledge into policy and practice.

Methods

WRF simulation framework. We employ the Weather Research and Forecasting (WRF, Version 4.4) model[76]—a physics-based mesoscale numerical weather prediction system widely used in atmospheric and urban climate research. Further details on WRF are provided in Supplementary Information. When coupled with urban canopy parameterizations, it enables the simulation of exchanges of momentum, heat, and moisture between the urban surface and the atmosphere, thereby providing a physically consistent framework to evaluate heat mitigation strategies under future climate scenarios. The physical parameterization schemes selected to align with validated approaches at similar scales[49,65], are described in **Supplementary Table 2**. To represent urban effects, we use the WRF model coupled with the building effect parameterization and building energy model (BEP/BEM)[77]. In this framework, local-scale processes including street-level airflow, radiative exchange, vegetation effects, and anthropogenic heat emissions generated by air conditioning systems are implicitly represented through the BEP/BEM[77] and land surface[78] parameterizations, which account for inter-grid variations in urban characteristics such as street layout, building height and density, albedo, heat storage, and vegetation fraction.

The model is applied to seven separate model domains (**Supplementary Fig. 11**) designed to cover 2,265 major cities across diverse climate zones worldwide. To balance the need for accurate representation of mesoscale atmospheric processes with computational efficiency, the model uses a horizontal grid spacing of 20 km and a total of 40 vertical atmospheric levels. Small cities occupying less than 20% of a WRF grid cell are considered to have a low urban impact and are therefore excluded from the analysis[79]. This configuration provides a robust representation of city-scale thermal and atmospheric processes, consistent with prior studies demonstrating its ability to capture the impacts of urban expansion, climate change and heat mitigation measures at the city scale[49,65,80]. The detailed model configuration and validation are illustrated in the Supplementary Information (WRF model configurations).

Datasets. The model is driven by the Bias-corrected Coupled Model Intercomparison Project Phase 6 (CMIP6) global dataset[81] under the high-emission, socioeconomically intensive scenario SSP 5-8.5, which represents the ensemble median within this scenario (**Supplementary Fig. 12**). This high-forcing scenario was selected as a stress-testing framework to evaluate the achievable urban cooling potential under the most extreme climate conditions[35,49,65]. The aim is to provide a conservative, risk-averse assessment that can serve as a benchmark for understanding the upper bounds of future urban cooling effectiveness and informing long-term planning under potential worst-case climate outcomes. To ensure a more robust and representative estimate, all simulations are conducted over three summer months for five consecutive years (from 2048 to 2052), covering June, July, and August in the Northern Hemisphere and December, January, and February in the Southern Hemisphere. Model outputs are archived at hourly intervals, with the first week (before

summer) of simulations excluded to allow for model spin-up. To further confirm the observed patterns, we repeated the simulations using the EC-Earth3 dataset, which represents the upper-bound case within the same scenario (**Supplementary Fig. 12**), and the results are shown in **Supplementary Fig. 2**.

The future urban land surface characteristics are determined by integrating the global urban land projection under the SSP5-8.5 scenario[82] with the present-day urban local climate zone (LCZ) map[83] at a 1 km resolution, which categorizes urban environments into eleven local climate zones based on their physical characteristics, such as building density, vegetation, and building heights[84]. Since the global urban land projection[82] primarily indicates the direction and intensity of urban expansion, we assume that newly urbanized areas inherit the LCZ type of the nearest existing urban area. This assumption draws on the neighborhood interaction concept, which has been extensively applied to describe spatial dependencies in urban expansion and land-cover change models[85]. With this approach, we produce a 1-km resolution projected LCZ map for the year 2050. Using LCZ-based urban canopy parameters[84], we subsequently compute the average urban canopy characteristics for each urban grid at the 20-km resolution employed in the WRF model, thereby assigning a unique set of urban canopy parameters to each grid cell to better represent the size and average morphology of the cities within it. A summary of this transformation for the simulation of the seven domains across the globe is provided in **Supplementary Figs. 13 and 14**.

Mitigation measures. Three physics-representative mitigation measures[28] are implemented in the model for all the urban grids. These simulation cases are designed to represent an ambitious yet plausible upper bound of achievable cooling potential under a consistent and comparable framework. Such generalized configurations are commonly adopted in large-scale urban climate modeling to isolate the physical mechanisms of heat mitigation and to provide a physically consistent benchmark for cross-regional comparisons[12,49,65,86]. The selected parameter values are informed by the basis of demonstrated effectiveness, technical feasibility, and consistency with prior studies. To further guide city-specific implementation of mitigation strategies, modeling that incorporates detailed urban morphology, surface material properties, vegetation, and related factors needs to be undertaken. Specifically, these measures include (1) green transformation (by restoring 30% of urban surfaces with natural surfaces[37,87]), (2) implementing reflective roofs and pavements (i.e., applying high-reflectivity materials with albedo = 0.5 and 0.88 for all pavements and building roofs, respectively)[23,24,88], and (3) reducing anthropogenic heat (i.e., raising the indoor temperature setpoint from 21 °C to 25 °C and improving the energy efficiency of air conditioning systems—specifically, by increasing the coefficient of performance (COP) from 3.5 to 4.5)[26,27,89,90].

To evaluate the full cooling potential of these measures, we assume an ambitious mitigation plan in which all building roofs and urban pavements are fitted with highly reflective materials and all building interiors are equipped with air conditioning systems operating at the adjusted setpoint

temperatures. Details on the implementation of these measures in the WRF model are provided in the **Supplementary Methods**. These measures and their parameter values are grounded in the established literature to reflect realistic and effective urban heat mitigation strategies widely supported by previous studies. The implementation of high-reflectivity materials—using high-albedo roof coatings (albedo = 0.88)[65] and stamped light concrete for pavements (albedo = 0.50)[91]—has been widely investigated in recent studies to assess their city-scale cooling effects across diverse urban climates[70,92–95]. The target urban green transformation level is informed by recent empirical findings suggesting that substantial cooling effects emerge once green cover approaches the 30-40% threshold range[67,96], which has consequently been adopted as a recommended target in urban forestry practice[97]. However, in practical applications, interventions like reflective materials may introduce unintended side effects—creating glare, increasing radiation exposure[69] and contributing to visual and thermal discomfort[98]—which should be carefully evaluated and addressed through innovative materials and designs[99,100]. Meanwhile, socioeconomic constraints, technological capability, and policy environment will play an indispensable role in shaping the applicability and scalability of such measures in practice.

While these three strategies are explicitly represented in the model, the physical mechanisms underlying other cooling interventions are also implicitly incorporated within these categories. For example, the enhancement of surface albedo through reflective roofs and pavements reflects the radiative benefits of adopting light-colored coatings and cool materials[62]. The green transformation category encompasses various forms of vegetation-based implementations, as well as the use of lightweight and low-heat-capacity building materials that reduce heat storage in urban areas[101]. Similarly, the anthropogenic heat reduction measure, evaluated through improvements in AC systems, indirectly represents the benefits of energy-efficient building design and the adoption of electrified transportation systems that reduce waste heat emissions[26].

Nevertheless, certain urban design-oriented cooling interventions—such as ventilation corridors and optimized urban layouts—can only be represented through their aggregated effects on surface roughness and heat exchange parameters, and thus cannot be fully characterized within this modeling framework[102]. Therefore, fully capturing the cooling benefits of such measures requires microscale modeling that resolves building-to-street scale aerodynamics[103] and associated ventilation processes[104].

Simulation setups. The simulation cases conducted are listed in **Supplementary Table 3**. By comparing the baseline cases (denoted I, no heat mitigation) with the combined heat mitigation cases (IV, incorporating green transformation, reflective roofs/pavements, and anthropogenic heat reduction), we calculate the urban cooling potential for each WRF simulation grid. To further evaluate the contribution of each individual heat mitigation measure, two additional cases are performed: (II) green transformation only and (III) green transformation combined with reflective

roofs and pavement. By comparing Cases I and II, II and III, and III and IV, we quantify the separate impacts of green transformation, reflective roofs/pavements, and anthropogenic heat reduction, respectively.

Assessment of heat stress. Heat stress arises from the combined effects of high air temperature and elevated humidity, which together impair the body's ability to dissipate heat through evaporative cooling. The heat content or moist static energy in the air can be measured by the equivalent temperature[31], $T_{eq} = T_a + e_a/\gamma$ where T_a is the 2-metre air temperature in degrees Celsius, e_a is the vapour pressure for the same height in hectopascals, and γ is the psychrometric constant (γ = 0.66 hope/K at sea level[58]). To quantify human heat stress, we use the wet-bulb globe temperature ($WBGT$), which is calculated at hourly intervals using the following empirical equation[105]: $WBGT = 0.567T_a + 0.393e_a + 3.94$. This index represents a weighted linear combination of an air–temperature component (T_a) and a humidity-related component (e_a/γ), reflecting the combined thermal and moisture-related burden on the human body. It is widely used in occupational health guidelines and climate-health research to assess the risks of heat-related illnesses and to set safety thresholds[106–108], allowing our findings to be directly linked to public health risk. Other heat indices, such as the wet-bulb temperature (T_w) and humidity index ($Humidex$), can also be expressed by the weighted linear combination of T_a and e_a/γ, with each index assigning different relative importance to these two components[18]. To evaluate how the results vary when alternative heat indices are applied, the cooling effects on both T_a and e_a/γ are presented in **Supplementary Fig. 10**, and the implications of these differences are further discussed in the discussion and conclusion sections.

Apart from temperature and humidity, human heat stress is also influenced by other meteorological and physiological factors including wind speed, radiation, clothing and metabolic rates[109]. The simplified wet-bulb globe temperature (WBGT) metric was developed to approximate outdoor thermal comfort under the assumption that other environmental and physiological factors remain constant[105]. It therefore isolates the combined influence of air temperature and humidity on human heat stress, providing a consistent and comparable indicator for large-scale assessments[31,106,110]. However, for assessments of heat risk focusing on microclimate—where wind dynamics and radiation exposure are critical—or on individual differences, where clothing, activity level, or heat tolerance play a role, more specialized heat indices could be considered[107,110].

Quantification of the urban cooling potential. The cooling potential for each city is quantified using the reduction in the five-summer average wet-bulb globe temperature ($\Delta WBGT$). To understand the influence of geographic latitude and background climate, cities are grouped by absolute latitude at 10° intervals. Consistent with previous findings that urban humid heat is strongly influenced by the precipitation regime[18,39], we further categorize them into wet and dry zones on the basis of summer precipitation thresholds (P_s=570 mm), which broadly separates

humid tropical climates from temperate and arid climates on the basis of the Köppen climate classification[18] (**Supplementary Fig. 15**).

Exposure to dangerous heat or heat extremes is assessed using summer heat danger hours (HDH), defined as the number of hours during the summer period that exceed the thermal danger threshold, which is calculated as $HDH_\theta = \sum_{i=1}^{n} 1(WBGT > \theta\ °C)$, where n is the total number of hours during the summer and where θ is the thermal danger threshold[32]. Two thresholds[32] are used in this study: the "danger" threshold (θ=31.4 °C), at which heat-vulnerable individuals are advised to avoid direct sun exposure and limit outdoor activities, and the "severe warning" threshold (θ=29 °C), at which all individuals are recommended to cease outdoor activities and seek shelter in air-conditioned areas[32]. We quantify the cooling potential of mitigation measures in reducing heat extremes by the percentage reduction in HDH, calculated as ΔHDH_θ in percentage $= \Delta HDH_\theta$ /baseline HDH_θ. The results determined with the "danger" and "severe warning" thresholds are presented in **Fig. 4** and **Supplementary Fig. 5**, respectively.

For each urban grid where the urban impervious fraction (UF_{grid}) exceeds 20%[79], $WBGT_{grid}$ and HDH_{grid} are calculated and averaged over all simulated summers. For cities spanning multiple WRF simulation urban grids, heat stress and exposure to heat extremes are represented by spatially weighted average values, which are calculated as follows: $WBGT = \sum(WBGT_{grid} * UF_{grid})/m$, $HDH = \sum(HDH_{grid} * UF_{grid})/m$, where UF_{grid} represents the urban fraction of each grid and where m is the total number of grids covering the city. The urban boundaries and geolocation information for identifying each city are from the Global Human Settlement (GHS) Urban Centre Database[111].

Diagnostics of heat flux changes driving the cooling effect. The surface energy balance (SEB) is a fundamental physical concept used in meteorology and urban climate studies to quantify energy exchanges between urban surfaces and the atmosphere[1,58,112]. We employ it as a diagnostic tool to identify and attribute the underlying drivers of cooling responses to heat mitigation measures[113]. The surface energy balance can be written as $A^* = R_n + Q_F + Q_G = Q_H + Q_E$ $(W \cdot m^{-2})$, where the available energy at an active urban surface (A^*)—compromising net radiation (R_n), anthropogenic heat (Q_F) and net heat storage in the urban fabric or ground heat flux (Q_G)—drives surface turbulent heat flux—sensible heat flux (Q_H) and latent heat flux (Q_E), which together represent the urban thermal environment[1]. Here, Q_G is considered positive when stored heat is released from urban surfaces to the atmosphere. The changes in each component of individual urban grids induced by the combined mitigation measures are shown in **Supplementary Figs. 7** and **8**.

Reducing the available energy at urban surfaces can directly lead to cooling. Compared with rural areas, urban environments typically exhibit latent heat flux (Q_E), characterized by a reduced

evaporative fraction[114] $\beta = Q_E/A^*$ (where $0 \le \beta \le 100\%$). This results in a larger proportion of available energy being converted into sensible heat (Q_H), which contributes to warming the lower atmosphere. Enhancing this fraction—such as through the implementation of green transformation—increases evaporative cooling and contributes to urban heat mitigation.

Following previous diagnostic frameworks[18,45,115], we employ a multiple linear regression approach to attribute the multiyear, summer-average cooling effect on $WBGT$ to the summer-average changes in the available energy components and evaporation fraction:

$$\Delta WBGT = a\Delta R_n + b\Delta Q_F + c\Delta Q_G + d\Delta\beta \quad (1)$$

where $a = \frac{\partial WBGT}{\partial R_n}$ (°C· $W^{-1} \cdot m^2$), $b = \frac{\partial WBGT}{\partial Q_F}$(°C· $W^{-1} \cdot m^2$), $c = \frac{\partial WBGT}{\partial Q_G}$(°C· $W^{-1} \cdot m^2$), and $d = \frac{\partial WBGT}{\partial \beta}$(°C per % change) are the sensitivities of $\Delta WBGT$ to changes in R_n, Q_F, Q_G and β. Δ denotes the difference in a given variable between the baseline case and the combined heat mitigation case.

The drivers of daytime and nighttime urban heat differ substantially. During the daytime, the surplus of all-wavelength radiation ($R_n > 0$) alongside anthropogenic heat ($Q_F > 0$) can be either convected into the lower atmosphere in the form of Q_H and Q_E or conducted into urban fabrics in the form of Q_G. At night, urban surfaces become net emitters of radiation ($R_n < 0$), and previously stored heat is released back to the atmosphere ($Q_G > 0$). To account for these two distinct processes, we develop corresponding regression models to diagnose the cooling effects during the daytime and nighttime via **Equation (2) and Equation (3)**. To enhance the physical realism of the models, we adopt two assumptions grounded in prior physical understanding to support the modeling framework. First, since changes in net radiation influence thermal conditions not only during the daytime (08:00-16:00) but also during transitional periods (4:00-8:00 and 16:00-20:00) and at night (20:00-04:00), we use the full-day average change in net radiation ($\Delta R_{n,A}$) in both regression functions. Second, given that anthropogenic heat and stored heat release during the nighttime influence the urban thermal environment through similar physical mechanisms[1], a shared regression coefficient is assigned to these two terms in **Equation (3)** to minimize multicollinearity and ensure model parsimony.

$$\Delta WBGT_D = a_1\Delta R_{n,A} + b_1\Delta Q_{F,D} + c_1\Delta Q_{G,D} + d_1\Delta\beta_D \quad (2)$$

$$\Delta WBGT_N = a_2\Delta R_{n,A} + b_2\Delta Q_{F,N} + b_2\Delta Q_{G,N} + d_2\Delta\beta_N \quad (3)$$

where the subscripts D, N, and A denote the daytime (8:00-16:00), nighttime (20:00-04:00) and 24-hour average values, respectively. a_1 - d_1 and a_2 - d_2 are the sensitivities of daytime $\Delta WBGT_D$ and nighttime $\Delta WBGT_N$, respectively. A summary of the data used to fit these two equations is presented in **Supplementary Fig. 7 and Fig. 8**, and the regression coefficients are shown in **Supplementary Table. 4.** The sensitivity to $\Delta\beta$ at night does not pass the significance

test ($p>0.001$) because the variation in this variable is much weaker than that in other variables, making it difficult to reliably assess its relationship with the dependent variable. The agreement between the modeled $\Delta WBGT$ and calculated $\Delta WBGT$ using linear regression is shown in both **Fig. 3** and **Supplementary Fig. 16**.

Data availability

The Bias-corrected can be accessed at https://www.scidb.cn/en/detail?dataSetId=791587189614968832. The EC-earth3 dataset are available at https://aims2.llnl.gov/search/cmip6/. The ERA5-Land hourly data are available at https://cds.climate.copernicus.eu/datasets/reanalysis-era5-single-levels?tab=overview.
The GHS built-up grid data are available at https://human-settlement.emergency.copernicus.eu/download.php?ds=smod. The weather station data for model validation are available at https:// www.ncei.noaa.gov/access/search/data-search/global-hourly.
The original LCZ-based land cover dataset is downloaded from https://zenodo.org/records/7670653. The future land cover projections are available at https://zenodo.org/records/4584775.

Code availability

The Weather Research and Forecasting (WRF) model can be downloaded from https://www.mmm.ucar.edu/models/wrf. The urban fraction and other urban parameters are calculated based on the WUDAPT-to-WRF python tool (https://github.com/matthiasdemuzere/w2w). The code used to generate the figures is available upon reasonable request. All statistical analyses and data visualizations were performed using the open-source Python (version 3.9.15) environment with the following packages: NumPy (v1.23.0), Pandas (v1.5.2), GeoPandas (v0.12.2), Matplotlib (v3.5.3), Cartopy (v0.22.0), PDAL (v2.4.3), PyProj (v3.4.1), W2W (v0.5.0), SciPy (v1.10.1), and Scikit-learn (v1.1.3).

Reference

1. Oke, T. R., Mills, G., Christen, A. & Voogt, J. A. *Urban Climates*. (Cambridge University Press, 2017).
2. Intergovernmental Panel On Climate Change. *Climate Change 2021: The Physical Science Basis. Contribution of Working Group I to the Sixth Assessment Report*. (Cambridge University Press, 2023).
3. Mora, C. *et al.* Global risk of deadly heat. *Nature Clim Change* **7**, 501–506 (2017).
4. *World Urbanization Prospects: The 2018 Revision*. (United Nations, New York, 2019).

5. Liu, J. *et al.* Rising cause-specific mortality risk and burden of compound heatwaves amid climate change. *Nat. Clim. Chang.* https://doi.org/10.1038/s41558-024-02137-5 (2024).
6. Jones, B. *et al.* Future population exposure to US heat extremes. *Nature Clim Change* **5**, 652–655 (2015).
7. O'Neill, B. C. *et al.* IPCC reasons for concern regarding climate change risks. *Nature Clim Change* **7**, 28–37 (2017).
8. Romanello, M. *et al.* The 2025 report of the Lancet Countdown on health and climate change. *The Lancet* https://doi.org/10.1016/S0140-6736(25)01919-1 (2025).
9. Tuholske, C. *et al.* Global urban population exposure to extreme heat. *Proc. Natl. Acad. Sci. U.S.A.* **118**, e2024792118 (2021).
10. Ebi, K. L. *et al.* Hot weather and heat extremes: health risks. *The Lancet* **398**, 698–708 (2021).
11. Wang, Y. *et al.* Global future population exposure to heatwaves. *Environment International* **178**, 108049 (2023).
12. Wang, S. *et al.* Dual impact of global urban overheating on mortality. *Nat. Clim. Chang.* https://doi.org/10.1038/s41558-025-02303-3 (2025).
13. Li, Y., Schubert, S., Kropp, J. P. & Rybski, D. On the influence of density and morphology on the Urban Heat Island intensity. *Nat Commun* **11**, 2647 (2020).
14. Zhao, Y. *et al.* Prioritizing Nature-Based Solutions and Technological Innovations to Accelerate Urban Heat Mitigation Pathways. *Annual Review of Environment and Resources* https://doi.org/10.1146/annurev-environ-111523-102159 (2025).
15. Grimmond, C. S. B. & Oke, T. R. Turbulent Heat Fluxes in Urban Areas: Observations and a Local-Scale Urban Meteorological Parameterization Scheme (LUMPS). *J. Appl. Meteor.* **41**, 792–810 (2002).
16. Li, D. *et al.* Urban heat island: Aerodynamics or imperviousness? *Sci. Adv.* **5**, eaau4299 (2019).
17. Manoli, G. *et al.* Magnitude of urban heat islands largely explained by climate and population. *Nature* **573**, 55–60 (2019).
18. Zhang, K. *et al.* Increased heat risk in wet climate induced by urban humid heat. *Nature* **617**, 738–742 (2023).
19. Krayenhoff, E. S. *et al.* Cooling hot cities: a systematic and critical review of the numerical modelling literature. *Environ. Res. Lett.* **16**, 053007 (2021).
20. Li, H. *et al.* Cooling efficacy of trees across cities is determined by background climate, urban morphology, and tree trait. *Commun Earth Environ* **5**, 754 (2024).
21. Qin, Y., Ghalambaz, S., Sheremet, M., Baro, M. & Ghalambaz, M. Deciphering Urban Heat Island Mitigation: A Comprehensive Analysis of Application Categories and Research Trends. *Sustainable Cities and Society* **101**, 105081 (2024).
22. Ürge-Vorsatz, D. *et al.* Locking in positive climate responses in cities. *Nature Clim Change* **8**, 174–177 (2018).
23. Santamouris, M. Cooling the cities – A review of reflective and green roof mitigation

technologies to fight heat island and improve comfort in urban environments. *Solar Energy* **103**, 682–703 (2014).

24. Raman, A. P., Anoma, M. A., Zhu, L., Rephaeli, E. & Fan, S. Passive radiative cooling below ambient air temperature under direct sunlight. *Nature* **515**, 540–544 (2014).
25. Seddon, N. Harnessing the potential of nature-based solutions for mitigating and adapting to climate change. *Science* **376**, 1410–1416 (2022).
26. Yuan, C. *et al.* Mitigating intensity of urban heat island by better understanding on urban morphology and anthropogenic heat dispersion. *Building and Environment* **176**, 106876 (2020).
27. Zhou, X. *et al.* Exploring the impacts of heat release of vehicles on urban heat mitigation in Sendai, Japan using WRF model integrated with urban LCZ. *Sustainable Cities and Society* **82**, 103922 (2022).
28. Akbari, H. & Kolokotsa, D. Three decades of urban heat islands and mitigation technologies research. *Energy and Buildings* **133**, 834–842 (2016).
29. Takebayashi, H. & Moriyama, M. Study on Surface Heat Budget of Various Pavements for Urban Heat Island Mitigation. *Advances in Materials Science and Engineering* **2012**, 1–11 (2012).
30. Rizwan, A. M., Dennis, L. Y. C. & Liu, C. A review on the generation, determination and mitigation of Urban Heat Island. *Journal of Environmental Sciences* **20**, 120–128 (2008).
31. Fischer, E. M. & Knutti, R. Robust projections of combined humidity and temperature extremes. *Nature Clim Change* **3**, 126–130 (2013).
32. Lin, Y.-C., Jung, C.-R., Hwang, B.-F. & Chen, C.-P. Investigating wet-bulb globe temperature on heat-related illness in general population for alerting heat exposure: A time-stratified case-crossover study. *Urban Climate* **59**, 102322 (2025).
33. Xu, Y. & Ramanathan, V. Latitudinally asymmetric response of global surface temperature: Implications for regional climate change. *Geophysical Research Letters* **39**, 2012GL052116 (2012).
34. He, C. *et al.* The effects of night-time warming on mortality burden under future climate change scenarios: a modelling study. *The Lancet Planetary Health* **6**, e648–e657 (2022).
35. Intergovernmental Panel On Climate Change (IPCC). *Climate Change 2022 – Impacts, Adaptation and Vulnerability: Working Group II Contribution to the Sixth Assessment Report of the Intergovernmental Panel on Climate Change*. (Cambridge University Press, 2023).
36. Wang, C., Li, Q. & Wang, Z.-H. Quantifying the impact of urban trees on passive pollutant dispersion using a coupled large-eddy simulation–Lagrangian stochastic model. *Building and Environment* **145**, 33–49 (2018).
37. Papangelis, G., Tombrou, M., Dandou, A. & Kontos, T. An urban "green planning" approach utilizing the Weather Research and Forecasting (WRF) modeling system. A case study of Athens, Greece. *Landscape and Urban Planning* **105**, 174–183 (2012).
38. Berardi, U., Jandaghian, Z. & Graham, J. Effects of greenery enhancements for the resilience

to heat waves: A comparison of analysis performed through mesoscale (WRF) and microscale (Envi-met) modeling. *Science of The Total Environment* **747**, 141300 (2020).

39. Zhao, L., Lee, X., Smith, R. B. & Oleson, K. Strong contributions of local background climate to urban heat islands. *Nature* **511**, 216–219 (2014).
40. Wienert, U. & Kuttler, W. The dependence of the urban heat island intensity on latitude A statistical approach. *metz* **14**, 677–686 (2005).
41. Su, Y. *et al.* Asymmetric influence of forest cover gain and loss on land surface temperature. *Nat. Clim. Chang.* **13**, 823–831 (2023).
42. Zhang, M. *et al.* Response of surface air temperature to small-scale land clearing across latitudes. *Environ. Res. Lett.* **9**, 034002 (2014).
43. Lee, X. *et al.* Observed increase in local cooling effect of deforestation at higher latitudes. *Nature* **479**, 384–387 (2011).
44. Yang, X., Li, Y., Luo, Z. & Chan, P. W. The urban cool island phenomenon in a high-rise high-density city and its mechanisms. *Intl Journal of Climatology* **37**, 890–904 (2017).
45. Yang, Y. *et al.* Regulation of humid heat by urban green space across a climate wetness gradient. *Nat Cities* https://doi.org/10.1038/s44284-024-00157-y (2024).
46. Vahmani, P., Luo, X., Jones, A. & Hong, T. Anthropogenic heating of the urban environment: An investigation of feedback dynamics between urban micro-climate and decomposed anthropogenic heating from buildings. *Building and Environment* **213**, 108841 (2022).
47. Haeffelin, M. *et al.* Impact of boundary layer stability on urban park cooling effect intensity. *Atmos. Chem. Phys.* **24**, 14101–14122 (2024).
48. Niu, G.-Y. *et al.* The community Noah land surface model with multiparameterization options (Noah-MP): 1. Model description and evaluation with local-scale measurements. *J. Geophys. Res.* **116**, D12109 (2011).
49. Wang, C., Wang, Z. & Yang, J. Cooling Effect of Urban Trees on the Built Environment of Contiguous United States. *Earth's Future* **6**, 1066–1081 (2018).
50. Meili, N. *et al.* Tree effects on urban microclimate: Diurnal, seasonal, and climatic temperature differences explained by separating radiation, evapotranspiration, and roughness effects. *Urban Forestry & Urban Greening* **58**, 126970 (2021).
51. Mughal, M. O., Li, X.-X. & Norford, L. K. Urban heat island mitigation in Singapore: Evaluation using WRF/multilayer urban canopy model and local climate zones. *Urban Climate* **34**, 100714 (2020).
52. Ferrando, M., Hong, T. & Causone, F. A simulation-based assessment of technologies to reduce heat emissions from buildings. *Building and Environment* **195**, 107772 (2021).
53. Ribeiro, F. N. D. *et al.* Impact of different transportation planning scenarios on air pollutants, greenhouse gases and heat emission abatement. *Science of The Total Environment* **781**, 146708 (2021).
54. Liu, Z., Ballantyne, A. P. & Cooper, L. A. Biophysical feedback of global forest fires on surface temperature. *Nat Commun* **10**, 214 (2019).

55. Seneviratne, S. I. *et al.* Investigating soil moisture–climate interactions in a changing climate: A review. *Earth-Science Reviews* **99**, 125–161 (2010).
56. Miralles, D. G., De Jeu, R. A. M., Gash, J. H., Holmes, T. R. H. & Dolman, A. J. Magnitude and variability of land evaporation and its components at the global scale. *Hydrol. Earth Syst. Sci.* **15**, 967–981 (2011).
57. Zhang, Y. *et al.* Global variation of transpiration and soil evaporation and the role of their major climate drivers. *JGR Atmospheres* **122**, 6868–6881 (2017).
58. Lee, X. *Fundamentals of Boundary-Layer Meteorology*. (Springer International Publishing, Cham, 2023).
59. Powis, C. M. *et al.* Observational and model evidence together support wide-spread exposure to noncompensable heat under continued global warming. *Sci. Adv.* **9**, eadg9297 (2023).
60. Sarkodie, S. A. & Strezov, V. Economic, social and governance adaptation readiness for mitigation of climate change vulnerability: Evidence from 192 countries. *Science of The Total Environment* **656**, 150–164 (2019).
61. Biardeau, L. T., Davis, L. W., Gertler, P. & Wolfram, C. Heat exposure and global air conditioning. *Nat Sustain* **3**, 25–28 (2019).
62. Santamouris, M., Synnefa, A. & Karlessi, T. Using advanced cool materials in the urban built environment to mitigate heat islands and improve thermal comfort conditions. *Solar Energy* **85**, 3085–3102 (2011).
63. Salamanca, F., Georgescu, M., Mahalov, A., Moustaoui, M. & Wang, M. Anthropogenic heating of the urban environment due to air conditioning. *JGR Atmospheres* **119**, 5949–5965 (2014).
64. Ding, X. *et al.* A WRF-UCM-SOLWEIG framework for mapping thermal comfort and quantifying urban climate drivers: Advancing spatial and temporal resolutions at city scale. *Sustainable Cities and Society* **112**, 105628 (2024).
65. Krayenhoff, E. S., Moustaoui, M., Broadbent, A. M., Gupta, V. & Georgescu, M. Diurnal interaction between urban expansion, climate change and adaptation in US cities. *Nature Clim Change* **8**, 1097–1103 (2018).
66. Gilabert, J. *et al.* Abating heat waves in a coastal Mediterranean city: What can cool roofs and vegetation contribute? *Urban Climate* **37**, 100863 (2021).
67. Jacobs, S. J., Gallant, A. J. E., Tapper, N. J. & Li, D. Use of Cool Roofs and Vegetation to Mitigate Urban Heat and Improve Human Thermal Stress in Melbourne, Australia. *Journal of Applied Meteorology and Climatology* **57**, 1747–1764 (2018).
68. Anand, J. & Sailor, D. J. How can we combine urban cooling strategies to effectively cool cities over the entire diurnal cycle? *Building and Environment* **242**, 110524 (2023).
69. Schneider, F. A., Ortiz, J. C., Vanos, J. K., Sailor, D. J. & Middel, A. Evidence-based guidance on reflective pavement for urban heat mitigation in Arizona. *Nat Commun* **14**, 1467 (2023).
70. Feng, J., Khan, A., Doan, Q.-V., Gao, K. & Santamouris, M. The heat mitigation potential

and climatic impact of super-cool broadband radiative coolers on a city scale. *Cell Reports Physical Science* **2**, 100485 (2021).

71. Morakinyo, T. E., Kong, L., Lau, K. K.-L., Yuan, C. & Ng, E. A study on the impact of shadow-cast and tree species on in-canyon and neighborhood's thermal comfort. *Building and Environment* **115**, 1–17 (2017).
72. Kubilay, A., Strebel, D., Derome, D. & Carmeliet, J. Impact of Tree Leaf Area Density on Cooling and Ventilation of an Urban Neighborhood. *J. Phys.: Conf. Ser.* **2654**, 012148 (2023).
73. Li, Y., Sun, Y., Li, J. & Gao, C. Socioeconomic drivers of urban heat island effect: Empirical evidence from major Chinese cities. *Sustainable Cities and Society* **63**, 102425 (2020).
74. Hsu, A., Sheriff, G., Chakraborty, T. & Manya, D. Disproportionate exposure to urban heat island intensity across major US cities. *Nat Commun* **12**, 2721 (2021).
75. Fung, K. Y., Yang, Z.-L., Martilli, A., Krayenhoff, E. S. & Niyogi, D. Prioritizing social vulnerability in urban heat mitigation. *PNAS Nexus* **3**, pgae360 (2024).
76. Skamarock, W. C. & Klemp, J. B. A time-split nonhydrostatic atmospheric model for weather research and forecasting applications. *Journal of Computational Physics* **227**, 3465–3485 (2008).
77. Ribeiro, I., Martilli, A., Falls, M., Zonato, A. & Villalba, G. Highly resolved WRF-BEP/BEM simulations over Barcelona urban area with LCZ. *Atmospheric Research* **248**, 105220 (2021).
78. Ek, M. B. *et al.* Implementation of Noah land surface model advances in the National Centers for Environmental Prediction operational mesoscale Eta model. *J. Geophys. Res.* **108**, 2002JD003296 (2003).
79. Demuzere, M., Argüeso, D., Zonato, A. & Kittner, J. W2W: A Python package that injects WUDAPT's LocalClimate Zone information in WRF. *JOSS* **7**, 4432 (2022).
80. Georgescu, M., Morefield, P. E., Bierwagen, B. G. & Weaver, C. P. Urban adaptation can roll back warming of emerging megapolitan regions. *Proc. Natl. Acad. Sci. U.S.A.* **111**, 2909–2914 (2014).
81. Xu, Z., Han, Y., Tam, C.-Y., Yang, Z.-L. & Fu, C. Bias-corrected CMIP6 global dataset for dynamical downscaling of the historical and future climate (1979–2100). *Sci Data* **8**, 293 (2021).
82. Chen, G., Li, X. & Liu, X. Global land projection based on plant functional types with a 1-km resolution under socio-climatic scenarios. *Sci Data* **9**, 125 (2022).
83. Demuzere, M., He, C., Martilli, A. & Zonato, A. Technical documentation for the hybrid 100-m global land cover dataset with Local Climate Zones for WRF. https://doi.org/10.5281/ZENODO.7670791 (2023).
84. Stewart, I. D., Oke, T. R. & Krayenhoff, E. S. Evaluation of the 'local climate zone' scheme using temperature observations and model simulations. *Intl Journal of Climatology* **34**, 1062–1080 (2014).
85. Van Vliet, J. *et al.* Measuring the neighbourhood effect to calibrate land use models. *Computers, Environment and Urban Systems* **41**, 55–64 (2013).

86. Georgescu, M., Broadbent, A. M. & Krayenhoff, E. S. Quantifying the decrease in heat exposure through adaptation and mitigation in twenty-first-century US cities. *Nat Cities* **1**, 42–50 (2023).
87. Li, X.-X. & Norford, L. K. Evaluation of cool roof and vegetations in mitigating urban heat island in a tropical city, Singapore. *Urban Climate* **16**, 59–74 (2016).
88. Li, D., Bou-Zeid, E. & Oppenheimer, M. The effectiveness of cool and green roofs as urban heat island mitigation strategies. *Environ. Res. Lett.* **9**, 055002 (2014).
89. Niamir, L., Ivanova, O., Filatova, T., Voinov, A. & Bressers, H. Demand-side solutions for climate mitigation: Bottom-up drivers of household energy behavior change in the Netherlands and Spain. *Energy Research & Social Science* **62**, 101356 (2020).
90. Creutzig, F. *et al.* Demand-side solutions to climate change mitigation consistent with high levels of well-being. *Nat. Clim. Chang.* **12**, 36–46 (2022).
91. Wang, C., Wang, Z.-H., Kaloush, K. E. & Shacat, J. Cool pavements for urban heat island mitigation: A synthetic review. *Renewable and Sustainable Energy Reviews* **146**, 111171 (2021).
92. Mohammed, A., Khan, A. & Santamouris, M. On the mitigation potential and climatic impact of modified urban albedo on a subtropical desert city. *Building and Environment* **206**, 108276 (2021).
93. Khorat, S. *et al.* Cool roof strategies for urban thermal resilience to extreme heatwaves in tropical cities. *Energy and Buildings* **302**, 113751 (2024).
94. Abraham, D. E. *et al.* Efficient outdoor thermal comfort via radiant cooling and infrared-reflective walls. *Nat Sustain* **8**, 642–650 (2025).
95. Anand, J., Sailor, D. J. & Baniassadi, A. The relative role of solar reflectance and thermal emittance for passive daytime radiative cooling technologies applied to rooftops. *Sustainable Cities and Society* **65**, 102612 (2021).
96. Ziter, C. D., Pedersen, E. J., Kucharik, C. J. & Turner, M. G. Scale-dependent interactions between tree canopy cover and impervious surfaces reduce daytime urban heat during summer. *Proc. Natl. Acad. Sci. U.S.A.* **116**, 7575–7580 (2019).
97. Konijnendijk, C. C. Evidence-based guidelines for greener, healthier, more resilient neighbourhoods: Introducing the 3–30–300 rule. *J. For. Res.* **34**, 821–830 (2023).
98. Synnefa, A., Santamouris, M. & Akbari, H. Estimating the effect of using cool coatings on energy loads and thermal comfort in residential buildings in various climatic conditions. *Energy and Buildings* **39**, 1167–1174 (2007).
99. Huang, X., Bou-Zeid, E., Pigliautile, I., Pisello, A. L. & Mandal, J. Optimizing retro-reflective surfaces to untrap radiation and cool cities. *Nat Cities* **1**, 275–285 (2024).
100. Rossi, F. *et al.* Radiative cooling improvement by retro-reflective materials. *Energy and Buildings* **336**, 115597 (2025).
101. Martins, T. A. L. *et al.* Impact of Urban Cool Island measures on outdoor climate and pedestrian comfort: Simulations for a new district of Toulouse, France. *Sustainable Cities*

and Society **26**, 9–26 (2016).
102. Li, X. *et al.* Meteorological effects of ventilation corridor in central urban areas: A case study of Wuhan. *Sustainable Cities and Society* **114**, 105752 (2024).
103. Zhang, J., Li, Z. & Hu, D. Effects of urban morphology on thermal comfort at the micro-scale. *Sustainable Cities and Society* **86**, 104150 (2022).
104. Carmeliet, J. & Derome, D. How to beat the heat in cities through urban climate modelling. *Nat Rev Phys* https://doi.org/10.1038/s42254-023-00673-1 (2024).
105. ABM. About the approximation to the WBGT used by the Bureau of Meteorology, Australia. Retrieved from http://www.bom.gov.au/info/thermal_stress/#approximation. (2010).
106. Parsons, L. A., Shindell, D., Tigchelaar, M., Zhang, Y. & Spector, J. T. Increased labor losses and decreased adaptation potential in a warmer world. *Nat Commun* **12**, 7286 (2021).
107. Budd, G. M. Wet-bulb globe temperature (WBGT)—its history and its limitations. *Journal of Science and Medicine in Sport* **11**, 20–32 (2008).
108. Epstein, Y. & Moran, D. S. Thermal Comfort and the Heat Stress Indices. *Ind Health* **44**, 388–398 (2006).
109. Fiala, D., Havenith, G., Bröde, P., Kampmann, B. & Jendritzky, G. UTCI-Fiala multi-node model of human heat transfer and temperature regulation. *International Journal of Biometeorology* **56**, 429–441 (2012).
110. Blazejczyk, K., Epstein, Y., Jendritzky, G., Staiger, H. & Tinz, B. Comparison of UTCI to selected thermal indices. *Int J Biometeorol* **56**, 515–535 (2012).
111. Kemper, T. GHS-UCDB R2024A - GHS Urban Centre Database 2025. European Commission, Joint Research Centre (JRC) https://doi.org/10.2905/1A338BE6-7EAF-480C-9664-3A8ADE88CBCD (2024).
112. Grimmond, S. Urbanization and global environmental change: local effects of urban warming. *Geographical Journal* **173**, 83–88 (2007).
113. Li, D. *et al.* Persistent urban heat. *Science Advances* (2024).
114. Gentine, P., Entekhabi, D., Chehbouni, A., Boulet, G. & Duchemin, B. Analysis of evaporative fraction diurnal behaviour. *Agricultural and Forest Meteorology* **143**, 13–29 (2007).
115. Zeng, Z. *et al.* Climate mitigation from vegetation biophysical feedbacks during the past three decades. *Nature Clim Change* **7**, 432–436 (2017).

Acknowledgements

We acknowledge Dominique Derome, Dominik Strebel, Haiwei Li, and Aytaç Kubilay for their valuable discussions during this research. Xiaotian Ding was supported by the Chinese Scholarship Council (No. 202306320335). The research was funded by funding from the National Natural Science Foundation of China (52578147) (Y.F.), "Pioneer" and "Leading Goose" R&D Program of Zhejiang (NO. 2023C03152) (Y.F.) and Zhejiang University-ETH Zürich Global Partnership

Fund (No. 100000-11320/209) (Y.F.). The SWEET-SWICE project funded by the Swiss Federal Office of Energy is acknowledged.

Author Contributions Statement

X.D., Y.Z. and Y.F. conceived and designed the study. X.D. conducted the simulations and analysis with the contributions from Y.Z., Y.F. and J.C.. X.D. wrote the original draft. Y.Z., Y.F., J.C., D. Ürge-V. and J.G. reviewed and edited the manuscript. All authors approved the final version of the manuscript.

Competing Interests Statement

The authors declare no competing interests.

Fig. 1. Spatial and diurnal patterns of heat extremes and the percentage mitigation potential offered by the combined mitigation strategy. a-d, Spatial distributions of the baseline heat danger hours (HDH) (**a, b**) and ΔHDH percentages (**c, d**) for world cities based on a wet-bulb global temperature ($WBGT$) danger threshold of 31.4 °C. **e**, Diurnal cycle of the mean baseline HDH (solid line) with the corresponding standard deviation (shaded area) for high-risk (right, 10° N-40° N) and low-risk (left, <10° N, >40° N) regions. **f**, The mean ΔHDH (solid line) and corresponding standard deviation (shaded area) in high-risk and low-risk regions; dashed lines indicate the percentage reduction in HDH relative to the mean baseline HDH; and tick marks for percentage values are referenced on the right vertical axis. Each box in panels (**b**) and (**d**) shows the median (horizontal line), mean (cross), interquartile range (box), and the 5th–95th percentile range (whiskers). The number of cities presented in each boxplot in panels (b) and (d) is listed in **Supplementary Table 1,** and no high-latitude cities ($|lat| > 30°$) in the dataset fall under the wet climate classification in this study.

Fig. 2. Asymmetric latitudinal patterns between the cooling potential and baseline urban heat stress. a-d, Cooling potential (**a, c**) and baseline heat stress conditions (**b, d**) during the daytime (**a, b**; 08:00–16:00 local time) and nighttime (**c, d**; 20:00–04:00 local time) across latitudinal bands and climate regimes. Each box presents the median (horizontal line), mean (cross), interquartile range (box) and 5th–95th range (whiskers). The number of cities presented in each boxplot is listed in **Supplementary Table 1,** and no high-latitude cities ($|lat| > 30°$) in the dataset fall under the wet climate classification in this study. The raw data underlying the statistical boxplots are presented in **Supplementary Fig. 4**.

Fig. 3. Primary drivers of daytime (a, 08:00–16:00 local time) and nighttime (b, 20:00–04:00

local time) cooling effects from combined heat mitigation measures. Boxplots represent the results from the Weather Research & Forecasting Model simulations (WRF), the calculated sum of each contribution (Cal.), and the estimated cooling effect from modifications in net radiation (ΔR_n)**,** anthropogenic heat (ΔQ_F), ground heat flux (ΔQ_G), and the ability of the urban surface to partition available energy into latent heat flux ($\Delta\beta$) aggregated over all urban grids (n = 4327). Each box presents the median (horizontal line), mean (cross), interquartile (box), and 5th–95th range (whiskers).

Fig. 4. Efficacy of individual mitigation measures in modifying surface energy balance components and enhancing cooling across latitudes and climates. The bar plots show the average contribution of each component to the cooling potential during the daytime (a–d) and nighttime (e–h), with different colors representing mitigation measures, including reflective surfaces, green transformation and anthropogenic heat reduction through air-conditioning system optimization (AC_{opt}). Darker shades represent dry climates, whereas lighter shades correspond to wet climates. The error bars indicate the mean cooling potential from combined mitigation measures, with standard errors calculated across urban grids. The number of urban grids presented in each boxplot is listed in **Supplementary Table 5,** and no high-latitude cities ($|lat| > 30°$) in the dataset fall under the wet climate classification in this study.

Editorial Summary:
A mismatch—salient across latitudes—between future urban heat risk and cooling potential reveals opposing patterns, with peak heat burden concentrated in lower-latitude regions, accentuating a clear imperative for context-specific adaptation strategies.

Peer review information: *Nature Communications* thanks Laura Carlosena, and the other, anonymous, reviewer(s) for their contribution to the peer review of this work. A peer review file is available.

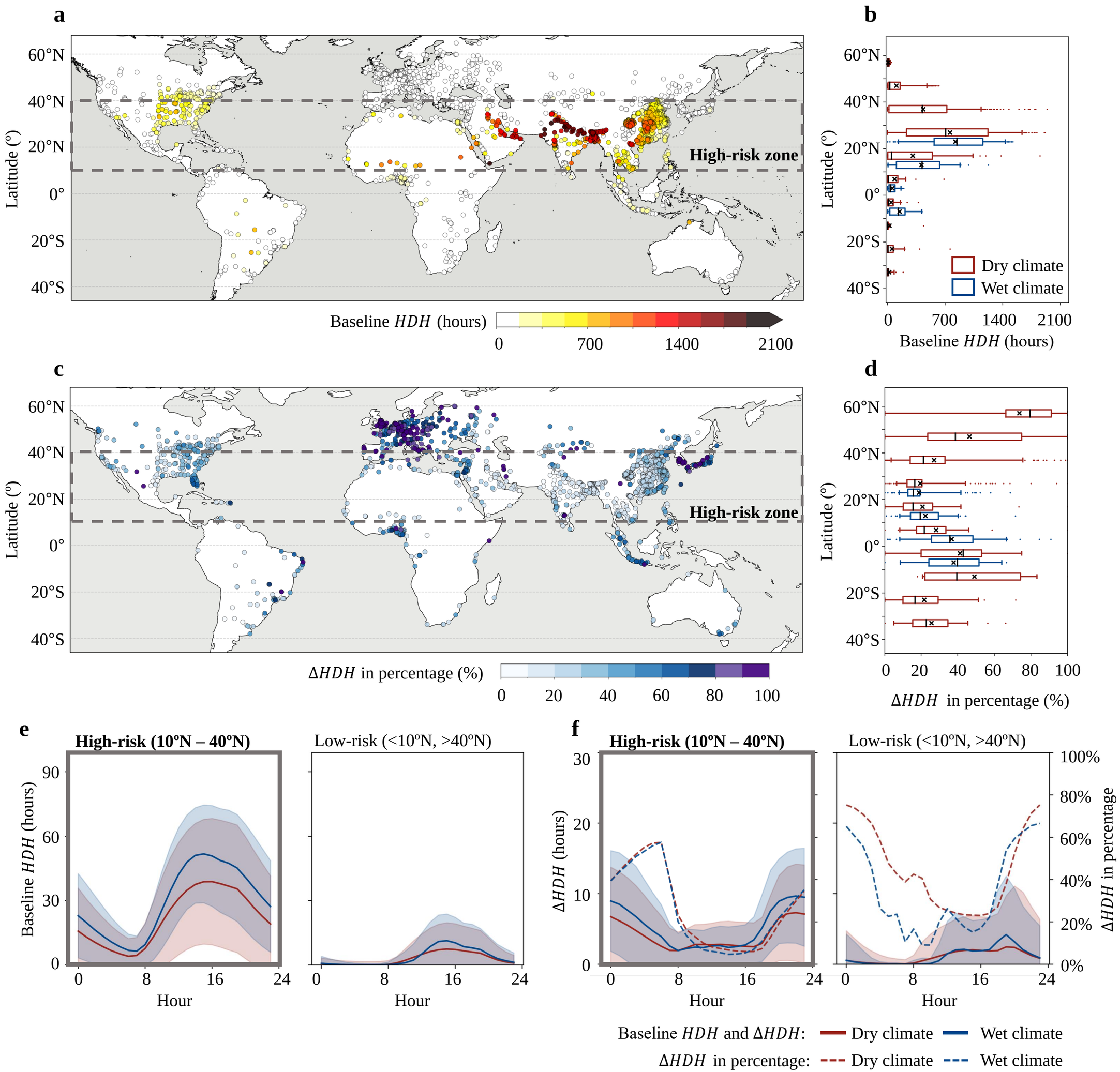
a
b
c
d
e
f
60°N
40°N
20°N
0°
20°S
40°S
Latitude (°)
High-risk zone
Baseline HDH (hours)
0
700
1400
2100
Dry climate
Wet climate
Baseline HDH (hours)
ΔHDH in percentage (%)
0
20
40
60
80
100
ΔHDH in percentage (%)
High-risk (10°N – 40°N)
Low-risk (<10°N, >40°N)
Baseline HDH (hours)
ΔHDH (hours)
ΔHDH in percentage
Hour
0
8
16
24
90
60
30
0
30
20
10
100%
80%
60%
40%
20%
0%
Baseline HDH and ΔHDH:
Dry climate
Wet climate
ΔHDH in percentage:
Dry climate
Wet climate

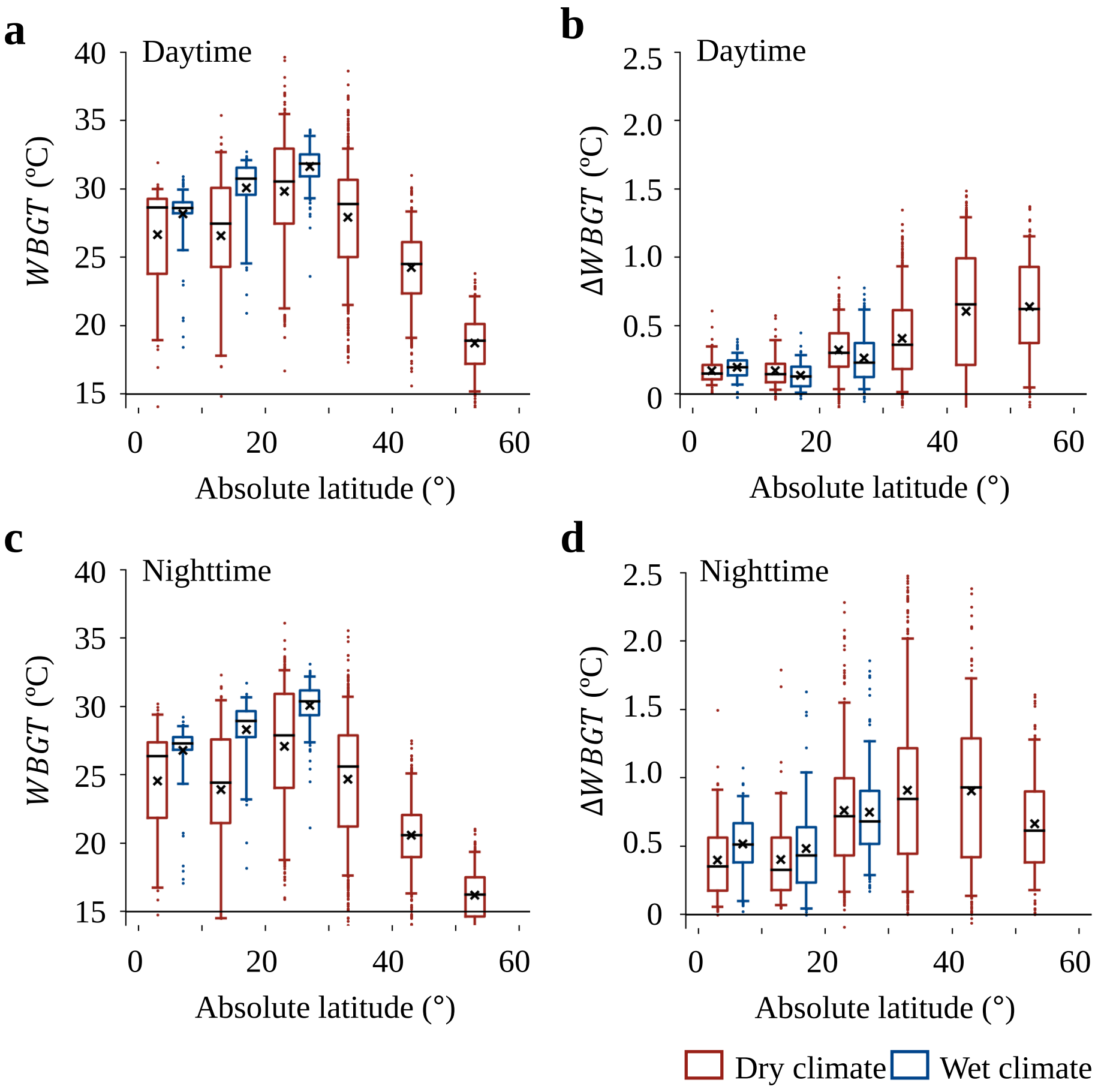
a
Daytime
WBGT (°C)
40
35
30
25
20
15
0
20
40
60
Absolute latitude (°)
b
Daytime
ΔWBGT (°C)
2.5
2.0
1.5
1.0
0.5
0
0
20
40
60
Absolute latitude (°)
c
Nighttime
WBGT (°C)
40
35
30
25
20
15
0
20
40
60
Absolute latitude (°)
d
Nighttime
ΔWBGT (°C)
2.5
2.0
1.5
1.0
0.5
0
0
20
40
60
Absolute latitude (°)
Dry climate
Wet climate

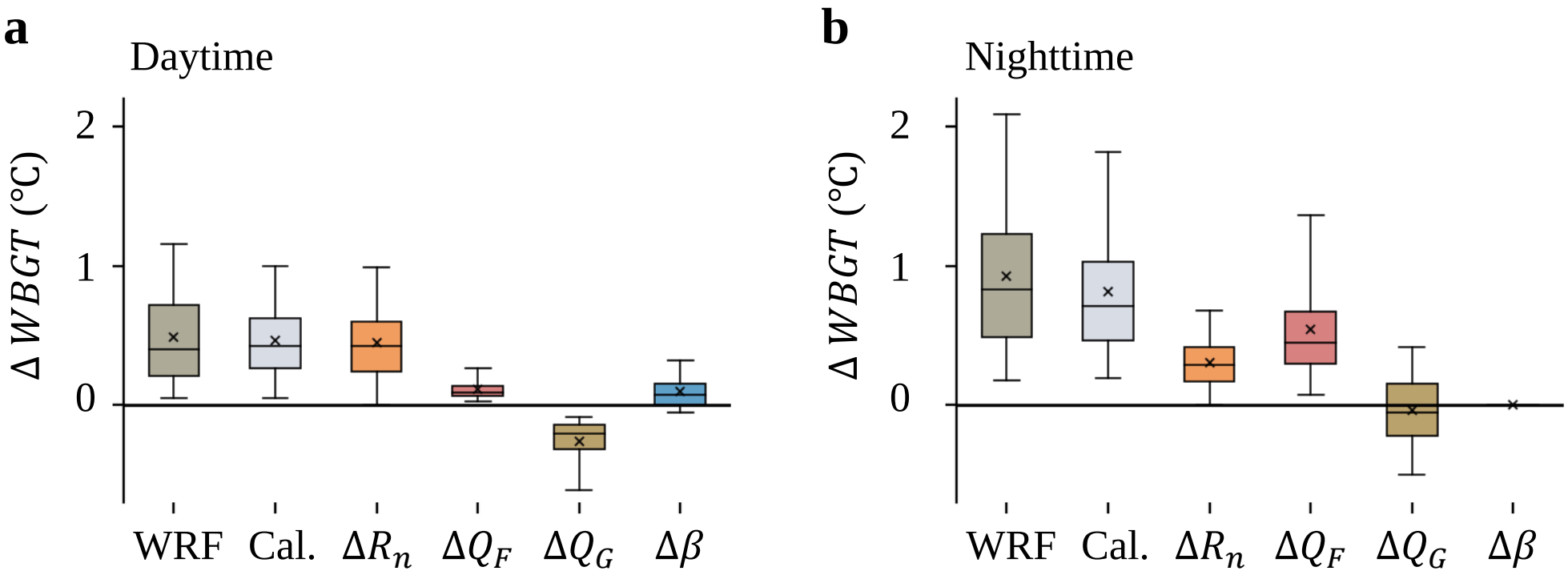
a
Daytime
b
Nighttime
$\Delta WBGT$ (°C)
2
1
0
WRF
Cal.
ΔR_n
ΔQ_F
ΔQ_G
$\Delta\beta$

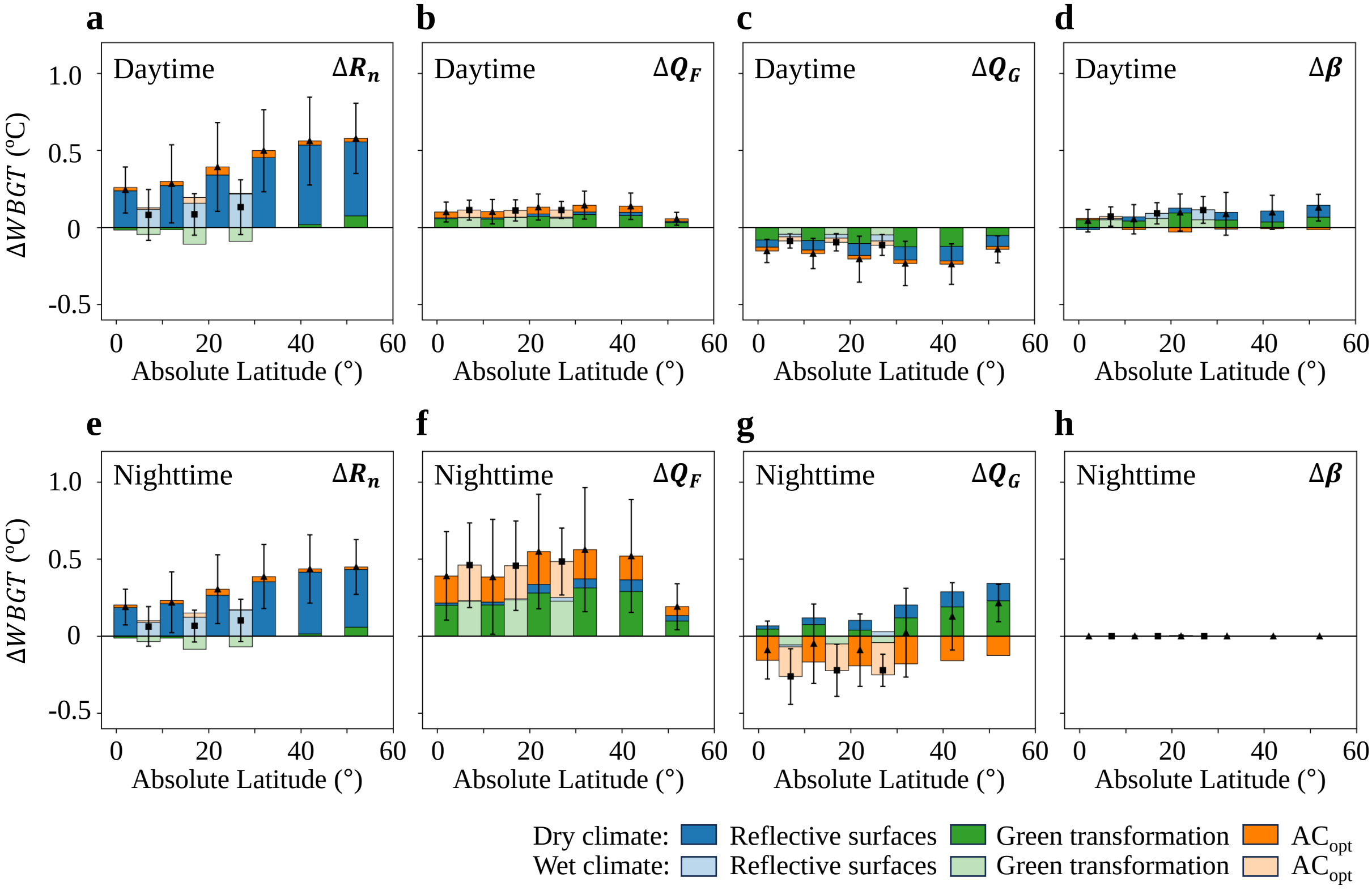
a
b
c
d
e
f
g
h
Daytime
Nighttime
ΔR_n
ΔQ_F
ΔQ_G
$\Delta \beta$
$\Delta WBGT$ (°C)
1.0
0.5
0
-0.5
0
20
40
60
Absolute Latitude (°)
Dry climate: Reflective surfaces
Green transformation
AC_{opt}
Wet climate: Reflective surfaces
Green transformation
AC_{opt}